AFRL-OSR-VA-TR-2013-0123

OPTIMIZATION OF A SMALL-SCALE ENGINE USING PLASMA ENHANCED IGNITON

Tonghun Lee

Michigan State University

March 2013
Final Report

AIR FORCE RESEARCH LABORATORY
AF OFFICE OF SCIENTIFIC RESEARCH (AFOSR)
ARLINGTON, VIRGINIA 22203
AIR FORCE MATERIEL COMMAND

REPORT DOCUMENTATION PAGE

Form Approved
OMB No. 0704-0188

PLEASE DO NOT RETURN YOUR FORM TO THE ABOVE ORGANIZATION.

1. REPORT DATE *(DD-MM-YYYY)*	2. REPORT TYPE	3. DATES COVERED *(From - To)*
12/31/2012	Final Report	01 October 2011 - 30 September 2012

4. TITLE AND SUBTITLE
OPTIMIZATION OF A SMALL-SCALE ENGINE USING PLASMA ENHANCED IGNITON

5a. CONTRACT NUMBER

5b. GRANT NUMBER
FA9550-10-1-0556

5c. PROGRAM ELEMENT NUMBER

6. AUTHOR(S)
Tonghun Lee

5d. PROJECT NUMBER

5e. TASK NUMBER

5f. WORK UNIT NUMBER

7. PERFORMING ORGANIZATION NAME(S) AND ADDRESS(ES)
Michigan State University
2555 Engineering Building
East Lansing, MI 48824-1226

8. PERFORMING ORGANIZATION REPORT NUMBER

9. SPONSORING/MONITORING AGENCY NAME(S) AND ADDRESS(ES)
Energy Conversion & Combustion Sciences Program (PM: Chiping Li)
Air Force Office of Scientific Research
875 North Randolph Street
Arlington VA 22203-1768

10. SPONSOR/MONITOR'S ACRONYM(S)

11. SPONSOR/MONITOR'S REPORT NUMBER(S)
AFRL-OSR-VA-TR-2013-0123

12. DISTRIBUTION/AVAILABILITY STATEMENT
Distribution A: Approved for public release

13. SUPPLEMENTARY NOTES

14. ABSTRACT

The research program described in this report is part of the AFRL Capstone efforts for undergraduate engineering students and is focused on studying the impact of using a plasma discharge system to enhance the combustion process in a small-scale internal combustion engine. The effects of two plasma systems were demonstrated using a small-scale engine (.1-100kW/USAF Unmanned Aerial Systems (UAS) Groups 1-3). The project was integrated into the Capstone undergraduate design program at Michigan State University as well as providing part support for graduate level research. In total, the project included the participation of eight undergraduate mechanical engineering students and the final research was exhibited by several of the students at the University Capstone Project Demonstration Day in the Small Engine Research Laboratory (SERL) at Wright Patterson Air Force Base in June, 2012.

15. SUBJECT TERMS
Plasma assisted combustion, laser diagnostics, direct coupling, microwave plasma

16. SECURITY CLASSIFICATION OF:			17. LIMITATION OF ABSTRACT	18. NUMBER OF PAGES	19a. NAME OF RESPONSIBLE PERSON
a. REPORT	b. ABSTRACT	c. THIS PAGE			Chiping Li
U	U	U	U	18	19b. TELEPHONE NUMBER *(Include area code)* 703-481-6930

Reset

Standard Form 298 (Rev. 8/98)
Prescribed by ANSI Std. Z39.18

Final Report

AFOSR Capstone Project:
OPTIMIZATION OF A SMALL-SCALE ENGINE USING PLASMA ENHANCED IGNITON

AFOSR Grant Number: FA9550-10-1-0556
Period of Research: 10/01/2010 to 9/30/2012

Submitted to:

The Air Force Office of Scientific Research
Energy Conversion and Combustion Sciences
Program Manager: Dr. Chiping Li

Tonghun Lee, Guoming (George) Zhu, Harold Schock
Department of Mechanical Engineering, Michigan State University

Corresponding PI: Tonghun Lee*

Department of Mechanical Engineering
Michigan State University
2555 Engineering Building
East Lansing MI 48824-1226
tonghun@msu.edu
(517)290-8005

November 2012

TABLE OF CONTENTS

1 ABSTRACT

The research program described in this report is part of the AFRL Capstone efforts for undergraduate engineering students and is focused on studying the impact of using a plasma discharge system to enhance the combustion process in a small-scale internal combustion engine. The effects of two plasma systems were demonstrated using a small-scale engine (.1-100kW/USAF Unmanned Aerial Systems (UAS) Groups 1-3). The project was integrated into the Capstone undergraduate design program at Michigan State University as well as providing part support for graduate level research. In total, the project included the participation of eight undergraduate mechanical engineering students and the final research was exhibited by several of the students at the University Capstone Project Demonstration Day in the Small Engine Research Laboratory (SERL) at Wright Patterson Air Force Base in June, 2012.

For the project itself, a dynamometer test stand with a test capacity of 7.0 kW was designed and built for testing a Fuji Imvac 34-EI single cylinder engine. The test rig monitors several engine parameters including engine speed, torque, air fuel ratio, cylinder head temperature, and in cylinder pressure. Two non-equilibrium plasma discharge systems were tested in the small engine and their effects on engine performance determined through comparison with a regular spark discharge (thermal discharge). One of the systems is a pulsed high quality radio frequency (RF) discharge and the other system is a commercially available nanosecond DC pulse plasma discharge system purchased from Plasmatronics LLC. Air fuel ratio (λ units are used in this report) sweeps were performed at several operating speeds to compare the ignition systems as a function of net indicated mean effective pressure (IMEP), the coefficient of variation of IMEP (COV_{IMEP}), and the maximum pressure rise rate of the averaged in cylinder pressure. The results show an improvement in power output, combustion stability, and tolerance of lean air fuel ratios ($\lambda > 1$) when the plasma systems are used. Additionally, optical engine measurements were conducted using the RF plasma discharge system which enhanced the lean flammability limit from $\lambda = 1.30$ with a standard coil to $\lambda = 1.45$ with the plasma. Images from the engine also show faster flame front propagation and a visually more intense reaction when the RF system is used.

2 INTRODUCTION

This proposal outlines an effort to characterize plasma ignition ranging from quasi to highly non-equilibrium discharges in a practical prototype small-scale engine. The study will involve development of a small engine test stand (7.0 kW) for accurate measurements of torque, power, air fuel ratio, and in-cylinder pressure. The main ignition system will be a high quality factor radio frequency (RF) ignition system for quasi-equilibrium plasma generation and a second optional system will be a nanosecond pulsed discharge for highly non-equilibrium plasma formation. In addition to the practical engine optimization, efforts will be made to (1) characterize the non-equilibrium nature of the plasma discharge, (2) investigate the ignition volume and flame propagation, and (3) measure changes in the combustion time period of the ignition system in an optical engine. *The novelty and significance is that it will be the first systematic interrogation of a plasma discharge with various degrees of thermal equilibrium both visually in an optical engine and also in a practical small scale engine*.

Plasma Energy Coupling for Combustion Enhancement

The advantages of combining electromagnetic radiation with combustion include faster and more intense combustion, increased stability in lean flammability limits, reduction of toxic combustion byproducts by altering oxidation chemistry, improved fuel efficiency by more complete combustion, more reliable and rapid ignition and fuel reformation [1-5]. Plasma energy can be used to energetically enhance combustion over a broader range of pressures (few Torr to tens of bar) and temperatures (500−3000 K).

Investigation of coupling electrical energy with combustion has a history of more than a century, with plasma discharge emerging as a source for enhancing combustion over the last four decades. Earlier studies improved combustion by applying an electric field [6-7], which was not strong enough to generate a plasma but altered the chemistry, flame stability, and flame propagation speeds. The first studies using a plasma discharge involved a thermal plasma jet to increase the flame speed and flammability limit of premixed flames [8-10]. While these new ignition systems proved to be much more effective than conventional spark plugs, the cost and complexity limited widespread use as an ignition source.

To date, various studies have been conducted to incorporate plasmas in flames for enhanced combustion. These studies have examined: pre-treatment of the fuel or reactants into hydrogen-rich syngas prior to combustion [11-12], enhanced ignition of hydrocarbon fuels [5,10,13], increased stability of combustion at atmospheric pressure [4,14-16] and enhanced combustion efficiency [17]. In particular, plasmas have shown great promise in improving the stability of high-speed ignition and combustion for supersonic propulsion systems [1,3,18-21], allowing for operation with greater efficiency, stability and power over a broad range of supersonic velocities. Plasma addition alters the reaction mechanisms by: (1) decomposition of the fuel gas from larger to smaller hydrocarbon molecules and radicals via the electron gas with temperature, T_e; (2) radiation-induced electron excitation [18]; (3) increased adiabatic flame temperature, T_{af}, that increases the rates of reaction and transport; and (4) impact of increased ion/electrons on key radical initiation and propagation reactions. More recently, plasmas have been identified as a main contributor for in-situ fuel reforming (resulting in syngas, H_2 and CO), which can greatly enhance the flame stability [22]. When plasma energy is coupled into the reaction zone of a flame as shown in Figure 1, a dramatic increase in electrons and ions impact the reaction pathways and increase the rate of chemical energy conversion.

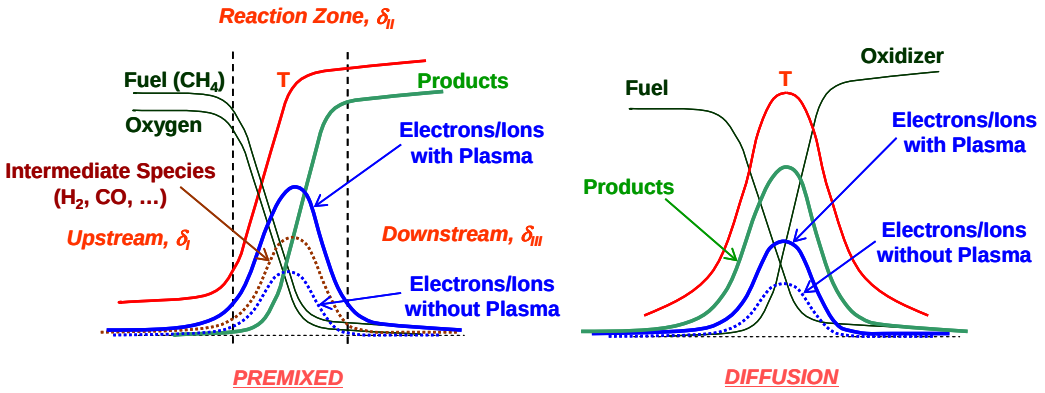

Figure 1 Combined flame and plasma in premixed and diffusion flames.

A number of different plasmas, including thermal plasma [19], dielectric barrier discharge [16], nanosecond pulsed discharge [13], pulsed corona discharge [23], RF discharge [17], DC or low frequency AC discharges [24], plasmatron [25] and microwave discharge [26] have been demonstrated in the laboratory. A more extensive review can be found in [2]. Plasma discharges have been used for enhanced ignition of internal combustion engines [27-28].

Quasi Non-Equilibrium Effects

The proposed work will use various degrees of 'non-equilibrium' plasma discharges which allow efficient energy transfer during the ignition. Purely thermal plasmas (*i.e.*, thermal arc, spark, *etc.*) have the disadvantage in that the main mode of energy transfer to the reactive mixture is via deposition of heat. In comparison, a non-equilibrium plasma, often called 'non-thermal' or 'low temperature' plasma, is characterized by internal energy modes (*i.e.*, rotational, vibrational and electronic temperatures) which deviate from a Boltzmann distribution and are different from the neutral gas temperature [29-30]. Temperatures of certain modes can be extremely high (thousands of K) while the rest of the system remains relatively cool (< 1000 K). In comparison, energy modes of typical combustion gases are in thermal equilibrium, where electrons, ions, radicals and background gases are at a similar temperature. This allows non-equilibrium plasmas to efficiently target energy transfer to specific degrees of freedom in the flame sensitive to acceleration of branching reactions and subsequent increase of flame speeds. Practical ignition systems for internal combustion engines are projected to be a quasi non-equilibrium system where both benefits of ohmic heating and non-equilibrium kinetic effects combined to synergistically enhance the ignition process.

Air Force Impact

The first impact is in the potential for miniaturization of combustion systems, particularly for development of small scale Unmanned Aerial Systems. Smaller combustion geometries inherently present higher surface area to volume ratios. The significant rise in heat transfer decelerates the chemical energy conversion rates, ultimately leading to flame extinction. Plasma ignition can offer unprecedented stabilization of the flame in these harsh conditions enabling highly advanced small scale propulsion systems as that required for unmanned aerial vehicles. The second significant impact of plasma enhanced combustion is in the development of next-generation supersonic airbreathing engines (*i.e.*, scramjet) which face significant technical challenges in flow control and combustion stability due to extremely high flow velocities. As a

result, window for stable combustion is narrow, and easily prone to acoustically generated oscillations and instabilities in combustion. The use of a non-equilibrium plasma discharge is a promising means of achieving both ignition and combustion stability under these extreme conditions. Third, plasma enhancement enables combustors to operate outside the normal flammability regime, such as ultra lean combustion for reduction of harmful byproducts. Finally, plasma technology can be a key technology for eventual expansion of a flexible fuel policy in the Department of Defense, enabling thermal oxidation of a heavy fuel such as JP-8 to be smoothly integrated over a wide range of advanced (including small-scale) internal combustion systems.

3 SMALL ENGINE TEST STAND

The Test Engine

The engine used in this study is a Fuji Imvac-34EI single cylinder, four stroke gasoline engine. The engine is sold for large scale model airplane applications popular with hobby enthusiasts. It also serves as the engine for the United States Air Force's Silver Fox remotely controlled aircraft. The engine has a 33.5 cc displacement, a compression ratio of 8.6, and bore and stroke of 39 x 28 mm. The engine has an advertised maximum power output of 2.0 hp, a maximum torque of 1.962 N-m, and a maximum operating speed of 7500 rpm. The engine has a single intake and a single exhaust valve. Fuel delivery for the engine is provided by a Walboro carburetor with high and low speed needle valve adjustments for tuning the air fuel. The engine is air cooled, and forced air is provided by an attached airplane propeller when the engine is used in its specified application. The engine uses an electronically controlled ignition system, called the EIS by Fuji, which utilizes a standard coil. The EIS system is powered by a 4.8 V rechargeable battery pack. The system uses a single pulse per engine revolution signal to control the triggering of the coil. The system adjusts ignition timing with engine speed, retarding the timing significantly at low speeds near idle and fires the system concurrent with the pulse signal at higher engine speeds. The crankshaft is accessible on both sides of the engine. The shaft protrudes farther on the output side of the engine and is tapered with a woodruff key and internally threaded center bore. A hub for attaching a propeller with a tapered bore and necessary keyway is provided with the engine. On the backside of the engine, there is a small protrusion of the shaft which has been cut with an external left handed thread.

The same basic engine is also sold in a package marketed for power equipment applications such as leaf blowers, weed trimmers, or fluid pumps as the Subaru/Robin EH035. This engine was also purchased for use in the project because its main components such as the cylinder head, valves, crankcase, piston, and crankshaft are identical to the Fuji's but sold at half of the cost. Also shortly after the start of this project, Fuji discontinued the Imvac line of engines. Photographs from Fuji's website and Subaru/Robin's website of the two engines are provided in Figure 1. The Subaru engine differs from the Fuji engine only in regards to its housing, the carburetor, the ignition system, and the accessories attached to the crank shaft. The Subaru engine comes equipped with a housing made of plastic that prevents users from contacting hot engine components. There are additional flanges and protrusions on the Subaru's cylinder head and crankcase casting that are clearly machined away from the Fuji engine's castings leading to the conclusion that both engines castings are identically sourced. The EH035's carburetor lacks the same adjustment capabilities provided with the Fuji engine. On the output side of the engine, the Subaru has a large flywheel that is bladed to provide forced air cooling and centrifugal clutch designed to engage at around 4000 rpm. A pull starter

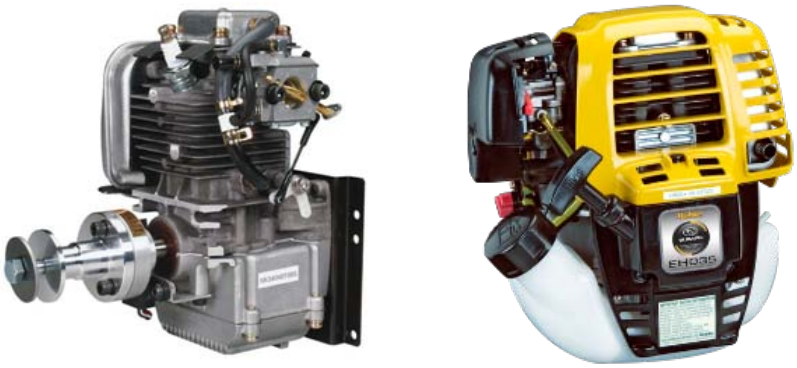

Figure 1 Fuji Imvac BF-34 EI and (right) Subaru EH035 Engines

is installed on the rear side shaft. With the clutch, flywheel, and pull starter removed, the crank shaft is identical to that of the Fuji engine with the same taper, key, and threads. The ignition system is a magneto coil attached to the flywheel. It is incapable of providing flexible ignition timing but does not require a separate power source. The peak power output of the Subaru is more modestly rated at 1.60 hp and 1.76 N-m of maximum torque. This is likely a result of the load added by the cooling fan blades on the flywheel and the disadvantage of using fixed ignition timing that is not necessarily optimized for peak power output.

While the Fuji version was the engine specified by the Air Force for this project, the Subaru engine is described above because the actual engine used for the testing presented in this report was performed using an engine whose base components were originally purchased as a Subaru engine. Its original carburetor was replaced with the carburetor from a Fuji engine and the EIS system was installed to serve as the engine's stock ignition system. With the plastic housing, clutch, flywheel, and pull starter all removed and the accessories just mentioned installed, the engine was effectively identical to a Fuji Imvac-34EI.

The Test Stand

One of the deliverables of this project is a small engine dynamometer test rig capable of accommodating internal combustion engines with up to 7.0 kW of power output. The test rig that was designed and built at Michigan State University is constructed on a platform of aluminum extrusions. The test stand is bolted together rather than welded so it can be disassembled and modified as needed in the future with simple hand tools. The aluminum profiles were selected because of their t-slotted profiles. The t-slots are the key to the rig's flexibility allowing its users to simply bolt on any needed additions whether it be additional instrumentation, engine hardware, or other auxiliary systems. The aluminum profiles support the dynamometer and its large aluminum base, which serves as the main test bed, that sits on vibration damping mounts secured to the structure. Mounting points are provided below the main structure for two blowers, one for cooling the dynamometer and one for cooling the small engine. Since the testing of the engine was performed in an open lab environment amongst other equipment and individuals, ½ inch thick impact rated polycarbonate protective windows were installed around the dynamometer test bed. The windows were easily removable and clamped into place to avoid creating noise from any vibration in the rig. The windows' supporting structure was modular; so if the rig were to be moved into a test cell, the entire window assembly could be removed with little effort and without affecting the base structure of the rig. The rig is equipped with large caster wheels that allow for it to be easily moved within the laboratory and leveling feet that can be lowered when a stationary location for the rig has been chosen. The overall dimensions of the test rig are roughly 35 x 63 x 69 inches. The test bed is elevated 36 inches from the ground and the protective class extends from several inches below this level up to 69 inch rig height. The aluminum base plate is 17 inches wide by 38.5 inches long and 2 inches thick. The end opposite of the dynamometer has a 15.5 inch long open surface with three t-slotted groves for engine mounting.

The test stand, shown in Figure 2, features a Magtrol ED-815 Hysteresis Dynamometer. This model dynamometer is rated to handle continuous engine power output of up to 8 hp and a five minute maximum power of 10 hp. The ED series of Magtrol dynamometers are designed to handle the high vibration of internal combustion engines. The dynamometer is relatively large compared to the test engine that has been selected in the study, but in order to deliver a test stand at the conclusion of the project close to the specifications desired for future use at Wright

Patterson Air Force Base, this size of dynamometer was required. The dynamometer uses a hysteresis brake that provides a frictionless torque loading that is independent of engine speed. The resistive torque provided by the dynamometer is generated by a magnetic field produced by a reticulated pole structure that restrains the rotor when energized. The torque is considered frictionless because there is no physical contact between the rotor and the stator of the dynamometer. A drawback to using a dynamometer with a hysteresis brake is that it cannot provide motive force to the engine; it can only provide a resistive torque.

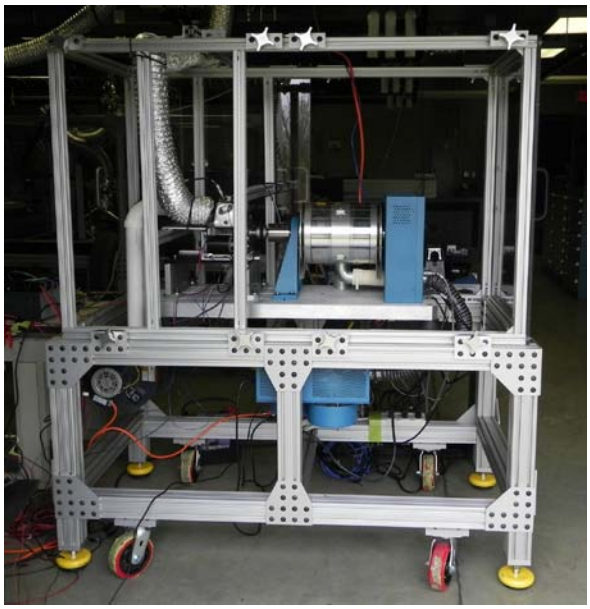

Figure 2 Small engine dynamometer test stand with protective windows removed.

The dynamometer is controlled using a Magtrol DSP6001 high-speed programmable dynamometer controller. The controller is designed specifically for use with Magtrol dynamometers. The controller has a built-in current-regulated power supply for energizing the dynamometer's hysteresis brake. The DSP6001 has adjustable proportional, integral, and derivative control gains to provide tuning for satisfactory torque or speed control accuracy and response from the dynamometer for a given engine setup. The controller can be controlled with its front panel or by a personal computer via an IEE-4888 (GPIB) interface. The GPIB provides 120 samples per second of speed and torque points. An auxiliary analog voltage output provides scalable torque, speed, and several alarm relays. These analog signals update every 2 ms and are sampled by the data acquisition system that will be described below.

The small-scale engine was mounted onto an aluminum L-bracket as shown in Figure 3. This bracket is designed to bolt onto an optical breadboard, an anodized plate with a gird of equally spaced threaded holes, has been elevated and precisely shimmed to provide a parallel surface to the dynamometer base plate. When the engine and its bracket are placed on the breadboard, the centerlines of the engine shaft and that of the dynamometer shaft lie in the same plane. The engine bracket was bolted to the breadboard through four slots running parallel to the engine's shaft using shoulder screws. The entire platform assembly was adjusted to position the engine and dynamometer

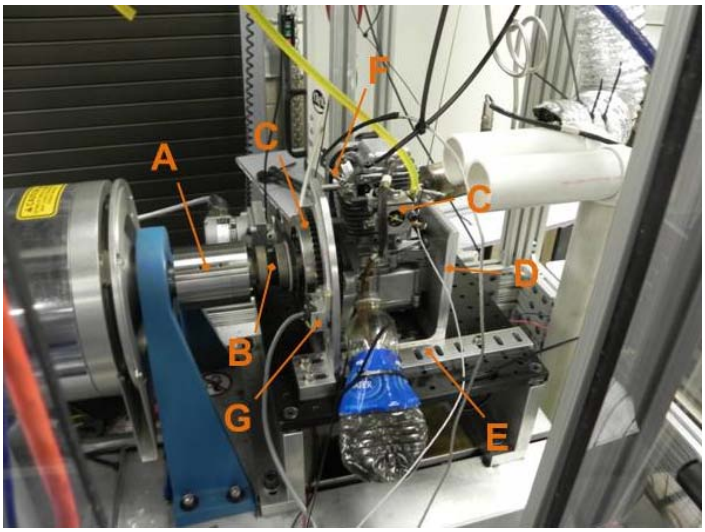

Figure 3 Photograph of installed engine taken from intake side: **A**) dynamometer shaft adapter, **B**) coupling, **C**) flywheels, D) engine mounting bracket, **E**) alignment block, **F**) in-cylinder pressure sensor, **G**) ignition timing Hall Effect sensor.

shafts into alignment. This alignment was verified using a dial gage attached to the dynamometer shaft that swept the outer diameter of the engine shaft. Once an acceptable alignment was achieved, the platform was bolted in place. A square plate was fastened to the optical plate while being pressed up against one of the sides of the engine bracket that runs parallel to the two shafts. The engine bracket can then be unfastened and slid backward and forward or removed from the rig. The engine is placed back into alignment simply by pushing the engine bracket back up against the alignment block. This allowed for easy removal of the coupling and other components of the shaft without the need to repeat the complete alignment process. The best alignment that was achieved produced a maximum offset of 0.020 inches between the shafts when swept by the indicator.

To complete the setup of the engine and in order to couple it to the dynamometer, several pieces of hardware were required to be fitted to both the engine and dynamometer shafts. A section view of the entire assembly of components connected to the engine and dynamometer shafts is shown in Figure 4. Since the dynamometer was incapable of motoring the engine, a 24 V DC electric motor was mounted next to the engine. A timing belt pulley (M in Figure 4) with a one way bearing (L) pressed into its bore was pressed onto a shaft extension (K) that was installed on the rear side of the engine's crankshaft and driven by the electric motor. The bearing was a CSK8P sprag element one-way roller bearing capable of transmitting 2.5 N-m of torque in the driving direction while generating a drag of only 0.8 N-cm when being overrun. This setup was capable of running the engine at up to 1600 rpm continuously for either acquisition of motoring data or starting the engine.

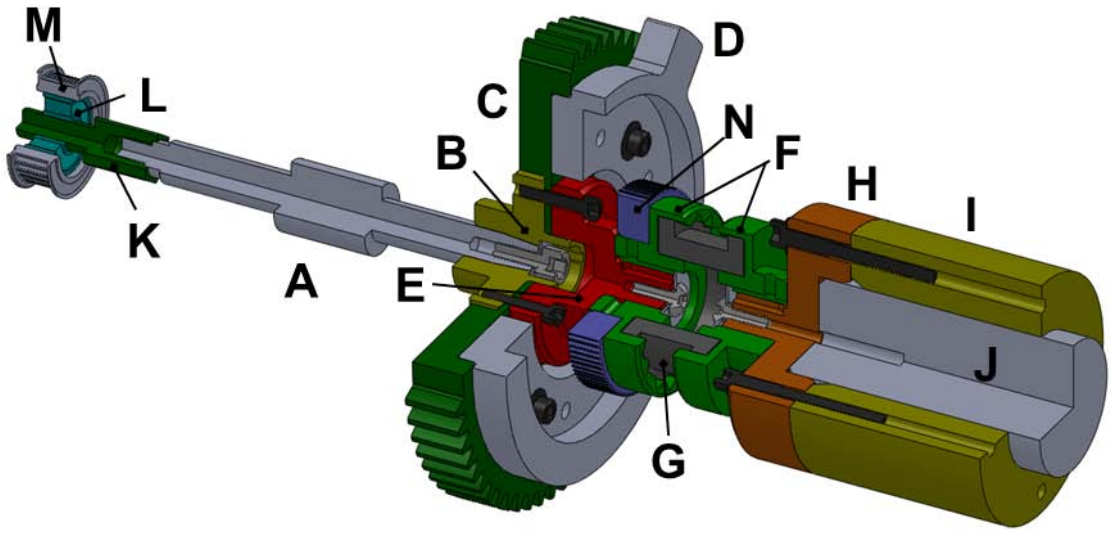

Figure 4 Quarter section view of engine shaft, dynamometer shaft, and associated hardware; body of the engine and dynamometer are not shown: **A**) engine shaft, **B**) engine hub, **C**) 60 minus 2 tooth spur gear flywheel, **D**) single tooth flywheel, **E**) engine shaft adapter, **F**) Martin Quadraflex coupling hubs, **G**) Martin Quadraflex coupling sleeve, **H**) dynamometer shaft adapter, **I**) keyed dynamometer collar, **J**) dynamometer shaft, **K**) rear side shaft extension, **L**) one-way bearing, **M**) starter timing belt pulley, **N**) encoder timing belt pulley.

Given the large disparity between the dynamometer's shaft size, 1.5 inches diameter, and the engine's shaft size, 0.155 inch diameter with a taper, several components were

fabricated to adapt the shafts to within the range of the bore diameter sizes of common couplings that suite the operating requirements of the test rig. There are two adapter hubs and two flywheels connected to the output side of the engine shaft. The first hub (B) has a tapered bore and keyway matching that of the small engine's shaft. The second hub (E) pilots on the first and provides a keyed ½ inch shaft for the hub of the coupling. Both flywheels provide substantial rotational inertia in order to help soften the effect of the harsh torque loads generated by the engine. The first of the two flywheels (C) is a modified 60 tooth 16 tooth per inch diametrical pitch steel spur gear with two adjacent teeth removed. A Hall Effect sensor is mounted next to the engine and senses each tooth as it passes by generating a quadrature like signal that is used by the control system to determine crank position. The second flywheel (D) is also steel and has a single square tooth that is sensed by a second Hall Effect sensor used to generate a single pulse per rotation signal. The purpose of this signal will be discussed below with the specifics of the control system. On the dynamometer side, a hub (H) that pilots on the dynamometer shaft provides the ½ diameter keyed shaft for the coupling and is bolted to a keyed collar (I) that transmits torque to the dynamometer's shaft.

A size 4 JEM Martin Quadra-flex coupling is used to couple the engine to the dynamometer. The coupling was selected for its tolerance of high misalignment and its torsional softness giving it the ability to tolerate the harsh vibrations generated by single cylinder engines. The coupling system consists of two metal hubs (F) with a thermoplastic rubber sleeve (G) spanning between them. The coupling is rated for a maximum speed of 7600 rpm and 13.6 N-m of torque. The specified allowable parallel and angular misalignments of the coupling are 0.010 inches and 1° respectively. While the actual misalignment achieved in the engine setup, as indicated above, exceeded these specifications, a coupling failure never occurred during testing and only a single coupling sleeve of this type was replaced during the lifetime of the project.

Figure 5 Martin Quadraflex coupling sleeve

Finally to complete the description of the test rig hardware, there are two blowers mounted beneath the level of the dynamometer base plate. The dynamometer is air cooled and comes equipped with its own blower which can be seen in Figure 2 located directly below the dynamometer. A second blower mounted below the engine side of the test bed blows air directed at the cooling fins of the engine to provide cooling.

Instrumentation

In cylinder pressure is measured using a Kistler Type 6052C piezoelectric pressure sensor. The 6052C is a front sealing sensor that is mounted in an M5 threaded counter bore machined into the cylinder head of the engine. The sensor lacks active cooling, but it is relatively insensitive to thermal effects, +/- 0.5% over the temperature range expected in the engine. The pressure sensor is connected to a Kistler Type 5010B Dual Mode Amplifier. The 5010B provides a voltage signal that is proportional to the cylinder pressure. The sensor is not absolute so it requires a reference pressure in order to be analyzed. In the processing of collected test data, the cylinder pressure was made equivalent to the reference pressure at bottom dead center (BDC) of the intake stroke of each engine cycle. In a large engine, the reference pressure is taken as the absolute pressure of the intake manifold. Since the testing performed in this study was all

completed at wide open throttle, the reference pressure used in analysis was the measured ambient pressure in the laboratory.

The air fuel ratio of the engine is monitored using an ECM AFRecorder 1200 system. The system consists of a sensor mounted in the exhaust system of the engine, a meter with a digital display and analog output, and its own power supply. The analog output signal is a programmable linearly scaled output of 0 to 5 volts. Its output ranged from λ = 0.4 at 0 volts and λ = 2 at 5 volts. The ECM sensor has its own heating element and is packaged similar to an oxygen sensor found on passenger vehicles. An extended exhaust pipe with a flange to accommodate the sensor was welded to the muffler of the engine. A probe for an OTC exhaust gas analyzer was also installed in this pipe. The analyzer was used to confirm that the ECM measurements were accurate. A photograph of the exhaust pipe with the installed sensor and analyzer probe are shown in Figure 6.

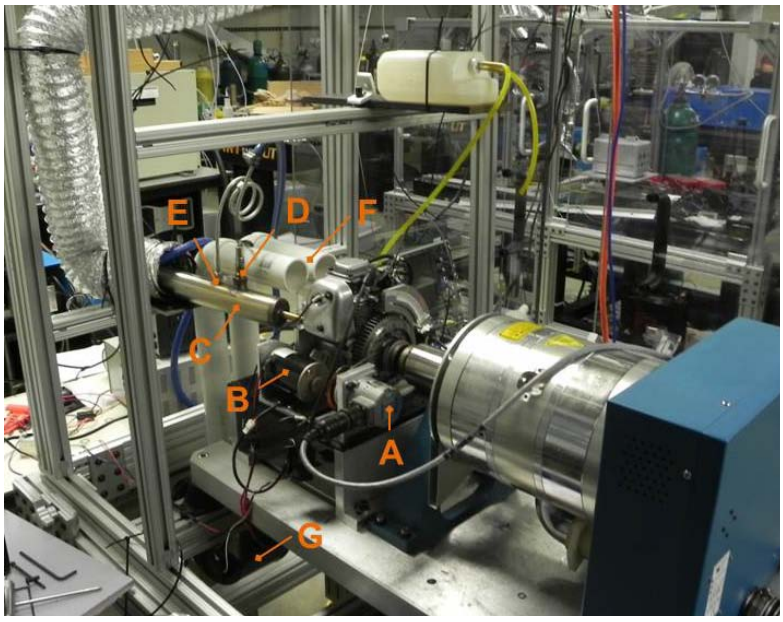

Figure 6 Test engine viewed from the exhaust side: **A**) BEI encoder, **B**) electric starting motor, **C**) extended exhaust pipe, **D**) ECM AFR exhaust sensor, **E**) OTC gas analyzer probe, **F**) blower ducts for engine cooling.

Crank position is measured using a BEI H25 incremental optical encoder. The encoder is a dual channel quadrature encoder with a third index channel and a 720 cycle per rotation resolution. Only a single encoder channel and the index channel were used in the analysis of the engine data collected to provide crank angle measurement in increments of ¼ of a degree. The encoder is coupled to the engine using two 90 tooth 2mm pitch synchronous timing belt pulleys. The setup uses a belt installed with high tension common among similar setups used in registration applications. The installed encoder is pictured in Figure 3.

Engine head temperature was monitored using an Omega SA1-RTD-B resistance temperature device (RTD). The RTD is read using an Omega HH804 Dual Input RTD Digital Thermometer. The RTD was surfaced mounted near the top of the engine cylinder on one of the engine's cooling fins. The cylinder temperature was not recorded with the test rig's data acquisitions system but used to determine that the engine had reached a steady operating temperature before data recordings were taken.

Engine Control System and Data Acquisition

Engine control was performed using a New Eagle Mototron Flash programmable ECU. The module controls throttle position and ignition timing. The Mototron control algorithm was designed at MSU and developed using MATLAB Simulink software and flashed to the ECU hardware. As mentioned briefly above, the controller uses the signal generated by a Hall Effect

sensor that picks up the passing teeth from a spur gear flywheel to determine crank position. Part of the Mototron's algorithm interprets the two tooth gap on the originally 60 toothed spur gear as an index for each engine rotation. The parameters of the controller and the desired engine speed are set using the LabView front panel shown in Figure 7 via of a National Instruments NI USB-8473 CAN module. This front panel also receives data from the dynamometer's GPIB device.

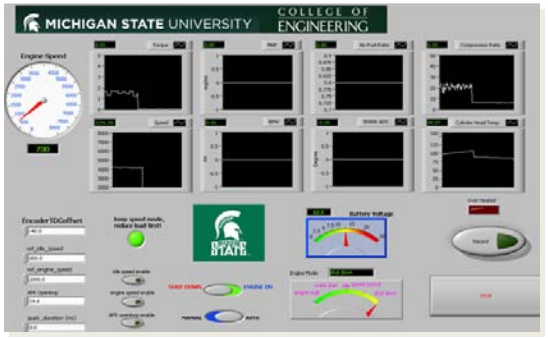

Figure 7 Mototron LabView front panel

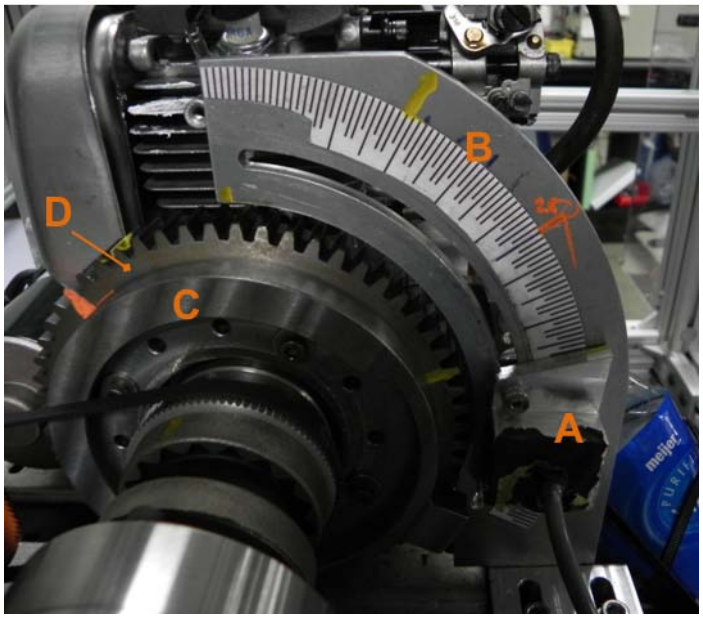

Figure 8 Alternative ignition triggering system; **A**) Hall Effect sensor, **B**) radial mounting track, **C**) single tooth flywheel, **D**) spur gear flywheel.

The RF plasma system created a large amount of electrical noise that interfered with the Mototron's ability to correctly interpret the crank signal generated by the spur gear flywheel preventing it from providing consistent ignition timing. An alternative ignition triggering system was developed to work around this issue. The system consist of a second flywheel with a single triggering tooth sensed by a second Hall Effect sensor mounted on a radial track as shown in Figure 8. The position of the sensor can be positioned manually along its track in order to adjust the engine's ignition timing. The falling edge of the signal generated by the flywheel tooth passing the sensor triggers a 555 timer based circuit that in turn sends the proper triggering signal to the RF plasma system.

Data acquisition is performed using a personal computer with a National Instruments multifunction DAQ PCI card, part number NI PC-6143. The device is a 16-bit resolution card with 8 analog voltage inputs that can be simultaneously sampled at a rate of up to 250 kHz at voltages within the range of +/- 5 V. The card is controlled using MATLAB's data acquisition toolbox and a MATLAB graphical user interface designed at Michigan State for the specific task of collecting data from the engine test stand. All eight of the channels are used for collection monitoring the three encoder channel outputs, analog speed and torque signals from the dynamometer controller, the analog output from the ECM exhaust sensor, and the triggering signal generated by the single tooth flywheel ignition timing system described above. The maximum sampling rate of 250 kHz rate was used in testing. The MATLAB program provided user inputs of test conditions and the sampling duration of each test.

Undergraduate Student Involvement

Two separate groups of undergraduate students were heavily involved in the development and construction of the small engine test stand under the supervision of Dr. Lee and a graduate

student. The first group was a design team of four students that worked on the project as the focus of their Capstone project during their final semester of school. The second group was composed of four students from Michigan State's Honors College that were selected as participants on this research project. The senior design project team was composed of students Curt Mumaw, Garret Kerns, Joseph Rotellini, and Stephen Santavicca. The Honors college team was composed of students Jonathan DiClemente, Tomas Hallahan, Gregory Tenbusch, and Adam Sajdak. The two teams are pictured below in Figure 9. As a collective group, these two student teams finalized the current project through their own creative designs as intended by the Air Force Capstone initiative.

Figure 9 Undergraduate student teams (left image, from left Dr. Lee, Joseph DiClemente, Tomas Hallahan, Daekeun Chun (graduate student), Adam Sajdak, Bryce Thelen (graduate student), Gregory Tenbusch) Honors college students (right image, from left Dr. Lee, Curt Mumaw, Garret Kerns, Joseph Rotellini, Dr. Naguib, Stephen Santavicca) Capstone Senior Design Team.

Figure 10 CAD model of Fuji Imvac-34EI engine modeled by one of the undergraduates.

During the spring 2011 semester, this project sponsored a group of ME 481 Senior Design Capstone students. The Capstone program at Michigan State University provides mechanical engineering seniors with the opportunity to implement their academic training in pratical exercises by participating in an industry funded design project. Each team of students is given a faculty advisor and an individual from their sponsoring company to help direct the team's effort. In this case, Dr. Ahmed Naguib served as the team's academic advisor while Dr. Tonghun Lee served as the sponsor advisor. The group was tasked with selecting an approriate dynamometer and the design and construction of the test rig. As part of the 481 program, the team met on a weekly basis with Dr. Naguib to discuss the project. The group also was responsible for writing two mid-term progress reports detailing their plans for the project, their design decsions, and any relevant analyses they produced throughout the semester. Each of these reports were presented to Dr. Lee in both written form and as presentations. The team's work culminatied with a final formal presentation at MSU's Design Day held on the final day of the semester in the Michigan State Student Union where the test rig that they had constructed was displayed.

Several of the members of Honors College group of students began their involvement with the project during the summer of 2011. The senior design group was unable to complete the test rig during their semester; so the second group assisted the graduate student in building up the test rig to an operational level and were involved in the troubleshooting of the initial engine testing. As intended, the final project was on dispay at the University Capstone Project Demonstration Day at Wright Patterson Air Force Base in June of 2012. A working model of the test rig was also on display at the Demonstration day as shown in Figure 11. Three of the students who participated on the project accompanied Dr. Lee on this trip.

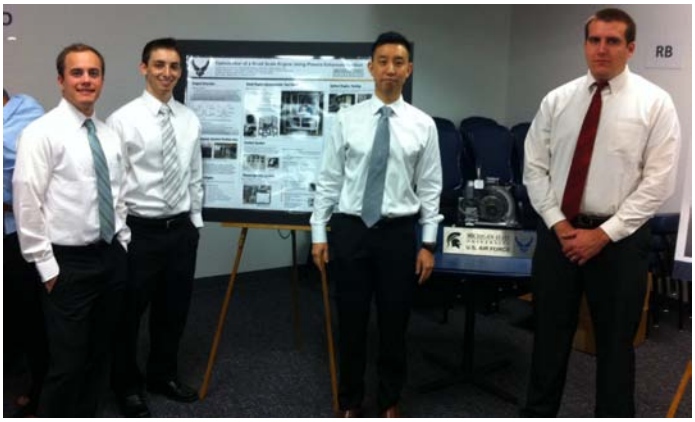

Figure 11 Photograph taken of the presenters at Demo Day

4 PLASMA ENHANCED IGNITION SYSTEMS

Three ignition systems were tested in the small engine. The standard coil EIS system that is sold with the Fuji engine was tested as a baseline for comparison to the plasma enhanced systems. The main focus of this study was centered on a radio frequency (RF) plasma discharge system designed at Michigan State University for use in this project. A third commercially available system was also purchased from Plasmatronics LLC.

The main component of the RF plasma system is a high voltage pulse generator. This pulsar provides a maximum voltage of 30 kV and is current limited at 200 mA. When firing, the generator pulses at a rate of 20 kHz, which is within the range of what is considered low radio frequency. These output pulses form a train composed of alternating high (30 kV) and low (0 V) voltage square waves of 25 µs width each. The voltage rise duration at 30 kV is 20 ns for each high voltage pulse. The maximum pulse train duration is limited to 1.2 ms. The generator was controlled using a 5 V TTL signal, firing during the duration of a low signal. The front of the generator is shown in Figure 12. The generator has a dial control for the adjustment of the high voltage output level as well as several analog voltage output BNC connections provided on the device to monitor its output. The system utilized the standard NGK CMR6A resistor spark plug that came installed in both the Fuji and Subaru engines. The generator connects to the spark plug using a non-inductive spark plug wire. As mentioned above, the RF pulsar generates a problematic amount of electrical noise. The steep high voltage rises generated by the device causes voltage spikes on inadequately shielded electronics while the pulsar fires. Adaptations to the ignition timing control, the processing of acquired data, and the addition of ferrite rings on the data acquisition computer's input devices were required as a result when testing with the RF system was performed.

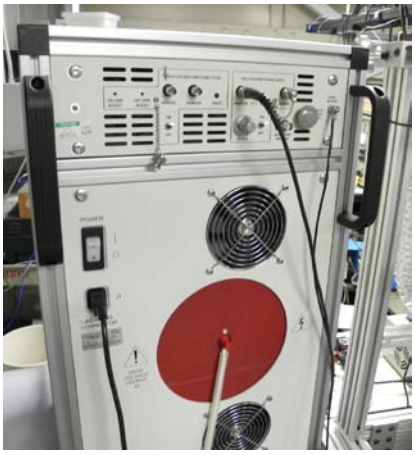

Figure 12 High voltage radio frequency pulsar

The second plasma system is a commercially available product adapted for use in the laboratory. The system, purchased from Plasmatronics LLC, is based on the company's Plasma Drive Ignition (PDI) module. The PDI is a direct current nanosecond discharge that produces a 20 ns pulse with a rise time of no more than 2 ns [31]. The module used has a variable voltage DC power supply and is capable of outputting voltages ranging from 13 to 57 kV to the spark plug. This system also uses the standard NGK spark plug and was controlled using a similar 5 V TTL signal, triggering on falling edges. Electrical noise was not a significant issue with this system. A photograph of the PDI module used in the testing is shown in Figure 13. This ignition system is referred to as the DC plasma system in the results section.

Figure 13 Plasmatronics PDI Module

5 SMALL ENGINE TESTING

Test Procedure and Data Analysis

Engine testing was performed at three engine speeds: 4000, 5000, and 6000 rpm. Each set of data was collected with the engine operating at wide open throttle (WOT). Data collection began only once the engine's cylinder head temperature reached a steady value. A sweep of λ values ranging from richer than λ = 0.9 up to the limit at which the engine no longer could sustain the desired operating speed were stepped through by adjusting the carburetor between acquisitions. Each acquisition lasted between 4.5 to 7.5 s depending on the engine speed. These sampling time durations were chosen such that each data point collected included over 200 engine cycles. Indolene was used as the fuel in all of the testing performed.

The net indicated mean effective pressure (IMEP) of the engine, the coefficient of variation (COV_{IMEP}) of IMEP, and the maximum pressure rise rate of the averaged cylinder pressure trace of the cycles collected in each acquisition were the focus of the engine testing. IMEP is calculated by integrating the measured cylinder pressure signal with respect to the cylinder volume over each cycle. The result of the integration is the net indicated work performed within the cylinder for the cycle. This work is divided by the cylinder displacement resulting in the mean effective pressure for each cycle. COV_{IMEP} is a measure of the variability of IMEP between separate engine cycles. By definition the COV_{IMEP} is the standard deviation of each cycle's IMEP in a given sample divided by the sample's mean value [32]. The pressure rise rate is indicative of the speed and intensity of combustion and is determined by calculating the derivative of the multi-cycle average cylinder pressure with respect to crank angle. In this study, a 3rd order finite difference formulation was used to compute this derivative from the discrete data collected.

The data collected for each test included dynamometer torque, dynamometer speed, λ, cylinder pressure, ignition control pulse and the three signals produced by the encoder. Each of the variables above was sampled at a rate of 250 kHz. The torque, speed, and λ data were analyzed as functions of time, while the cylinder pressure and ignition control pulse were resolved using one of the main encoder channels and the encoder index into functions of crank angle with a resolution of ¼ of a degree. The speed, torque, and λ data were averaged over the testing sample. A measure of the variability of λ for each test was also calculated as inconsistent

fuel delivery adversely affected the data collected on occasion, particularly in regards to the COV_{IMEP}, and data points exhibiting a large amount of variability in λ were discarded

The ignition timing of the standard EIS provided with the Fuji engine was unaltered during testing. It is assumed that this system has been setup to run with optimal timing at near stoichiometric air fuel mixtures. For the two plasma systems, ignition timing was determined for each system at each testing speed by performing a timing sweep with λ held at unity. The resulting break torque vs. timing angle curves were used to find the timing that yielded maximum torque for each system at each testing speed. The timing determined at λ =1 was used for the entire set of testing at each respective engine speed throughout the λ sweeps. This is done because the timing of the standard ignition system was not altered and adjusting the timing of the plasma systems as λ was varied such that engine would always operate at minimum advance for best torque (MBT) would not provide a good comparison of the plasma systems with the standard coil. Examples of the timing sweeps for the RF plasma at 4000 and 6000 rpm are shown in Figure 14.

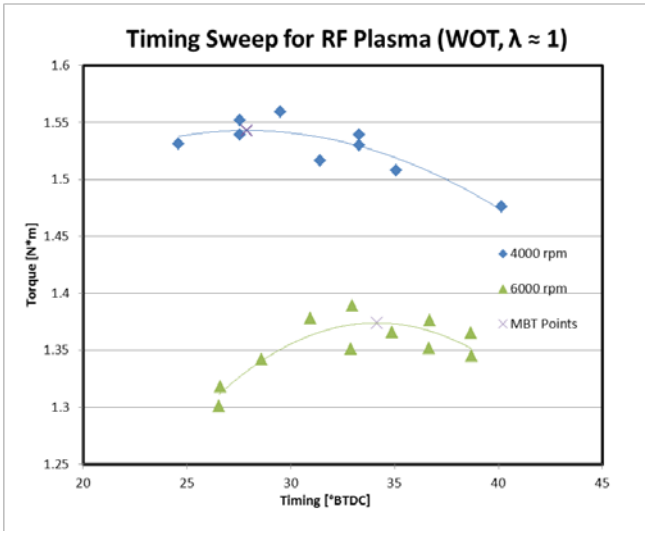

Figure 14 Timing Sweep results used to determine MBT for RF Plasma system at λ=1.

An accounting of the noise generated by the RF system was required during processing of the data collected from tests conducted with the system. While the encoder signals were immune to the noise, the analog signals generated by the dynamometer controller and ECM exhaust gas sensor were strongly affected. The pressure sensor was generally unaffected, but on occasion it would pick up the noise and overload the charge amplifier causing it to cease operation. A sample of one of the plots generated during the processing of the data collected from an RF system test is shown in Figure 15. The plot displays raw speed and pressure signals collected for the test. The pressure signal is displayed to confirm that the charge amplifier did not malfunction during or prior to the test while the speed signal shows the extent of the noise present on that channel. The control of such noise would become a major issue for plasma ignition systems if they are to one day become a mainstay of internal combustion engines on a larger scale.

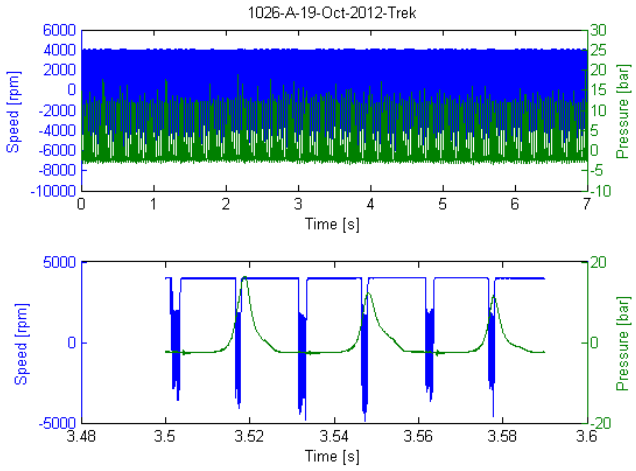

Figure 15 Sample of raw data collected from test run with RF Plasma

The affected speed, torque, and λ signals are all time based and averaged for each acquired data point. Without removing the noise affected regions in the data, values of the averaged quantities were at a minimum 90% of their true values. Therefore, an algorithm was developed and implemented as part of the data processing routine for the data collected from tests with the RF system to remove the noise corrupted regions of the three time based signals. Since engine speed is the set variable that is actively controlled by the dynamometer in all of the tests, it has relatively stable values throughout each acquisition and was the parameter used to detect the noise affected sections of the data. When the RF system is fired, the speed signal drops sharply. After the system has stopped firing, the signal rebounds and settles back to the mean speed, but it does so at much less pronounced rate then it does when the deviation began. The noise removal algorithm takes the mean value of the raw speed signal and subtracts it from the speed signal generating a measure of the deviation from the mean quantity. This deviation is then scanned in the direction of increasing time with the algorithm detecting where the deviation exceeds an absolute value of 200 rpm. Since the effects of the noise are very abrupt at the onset of noise affection, the starting location is easily identified. A span of around 2.5 ms of data is then removed from the three signals and the algorithm begins searching for the next large deviation. Figure 16 displays a plot of two noise events in the sample test shown in Figure 15. The green vertical lines mark the beginning and the red vertical lines the end of the segments of data that are removed from the speed, torque, and λ signals of the test.

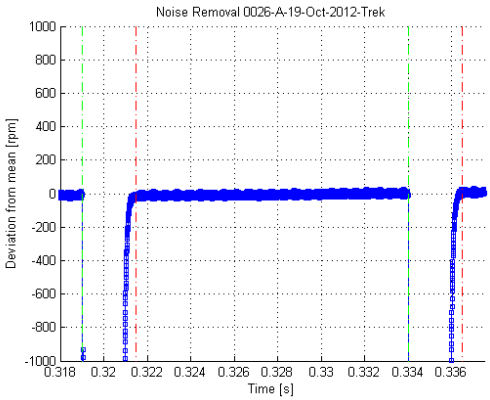

Figure 16 Example of the noise removal process using the analog speed signal provided from the dynamometer.

Test Results

The following results were all collected with the engine running at a steady temperature at WOT. The RF high voltage pulsar was set to an output voltage of 30 kV with a pulse train duration of 1.2 ms and MBT ignition timing determined at λ = 1. The Plasmatronics PDI module was set to output at 57 kV with ignition timing also determined at λ = 1. Plots displaying average IMEP, COV_{IMEP}, and pressure rise rate as functions of λ are shown in Figures 17, 18, and 19 for tests conducted at 4000, 5000, and 6000 rpm respectively. The Plasmatronics PDI module was tested only at 5000 rpm.

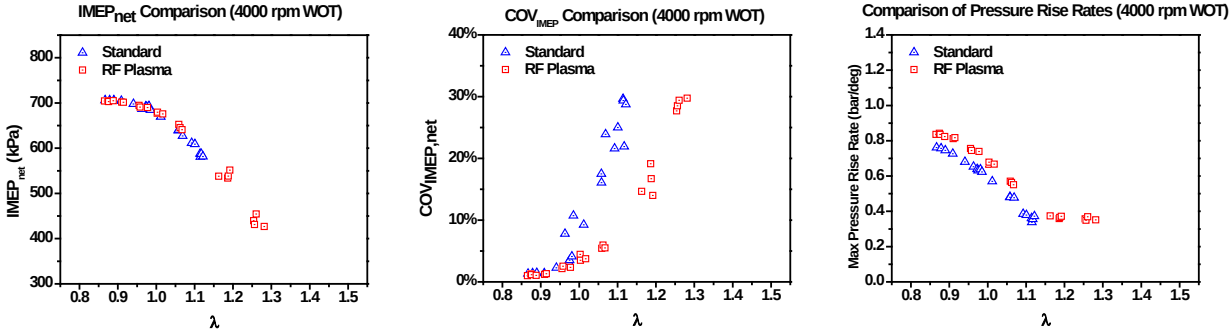

Figure 17 Results of AFR sweep WOT at 4000 rpm

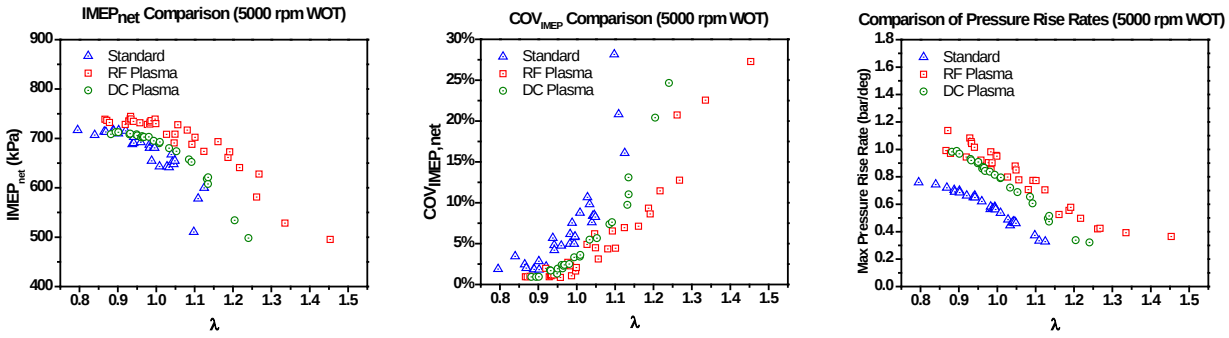

Figure 18 Results of AFR sweep WOT at 5000 rpm

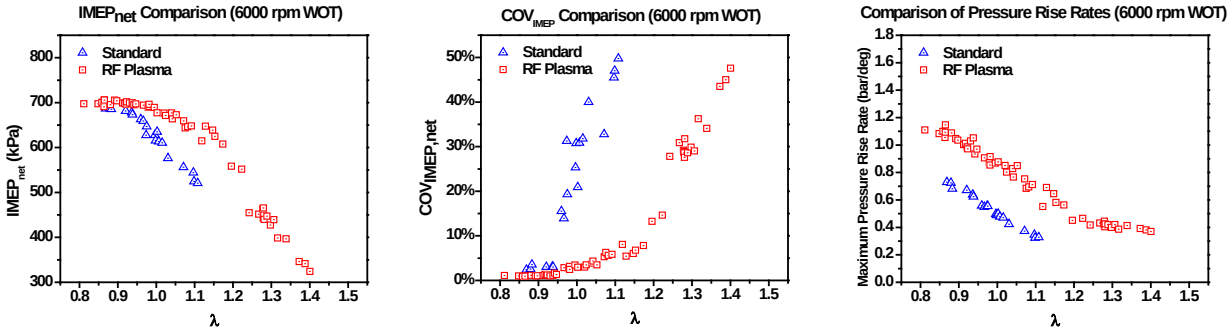

Figure 19 Results of AFR sweep WOT at 6000 rpm

Examining the data presented above in the average IMEP comparisons, it is clear that the plasma enhanced systems provide higher engine power output than the standard coil at identical λ. The improvement becomes more pronounced as λ increases into the lean region of combustion and as the engine speed increases. The same pattern is observed in the COV_{IMEP} comparison plots. At identical λ, the plasma systems provide more stable, lower values of COV_{IMEP}, combustion than the standard coil. Again as λ is increases into the lean region, the difference between the systems becomes more significant. Clearly, these plots indicate an enhanced ability for the engine to run using lean air fuel mixtures. It is also worth noting that in the 5000 rpm tests the Plasmatronics DC plasma shows similar improvement, but the improvement is slightly inferior to that of the RF system.

The impact can be more fully appreciated by looking at two specific data points. For example, the 6000 rpm operating speed data set for the EIS system includes a test point at λ = 1.00 with an IMEP of 634 kPa. At the same operating speed with the RF plasma system, a point with a similar output of 639 kPa is achieved at λ = 1.147. Not only is the power output nearly identical at the leaner mixture, the COV_{IMEP} is also improved from 21% for the standard system at λ = 1 down to 6.0% at λ = 1.147 for the RF plasma system. COV_{IMEP} values lower than 6.0% are not seen with the standard coil after λ becomes greater than 0.94 at 6000 rpm.

Insight as to why the output of the engine is higher with the plasma systems can be gained by examining the third plot in each of the three figures that compare the maximum pressure rise rates of each system. It is clear in these plots that the pressure rise rate is always higher for the plasma system. This suggests that the rate of combustion is more rapid when these systems are

used. The increased pressure rise rate leads directly to higher cylinder pressures earlier in the expansion stroke resulting in a higher output. The effects of the enhanced rate of combustion are more pronounced as engine speed increases, which results in a reduction in the amount of time that the mixture has to burn, and as the air fuel mixture becomes leaner, which causes a decrease in flame speed.

Finally, Figure 20 displays averaged pressure traces for data points at $\lambda = 1$ for all three of the engine speeds tested. The trends in these three plots further demonstrate that the improvement effects of the plasma are more pronounced as engine speed increases.

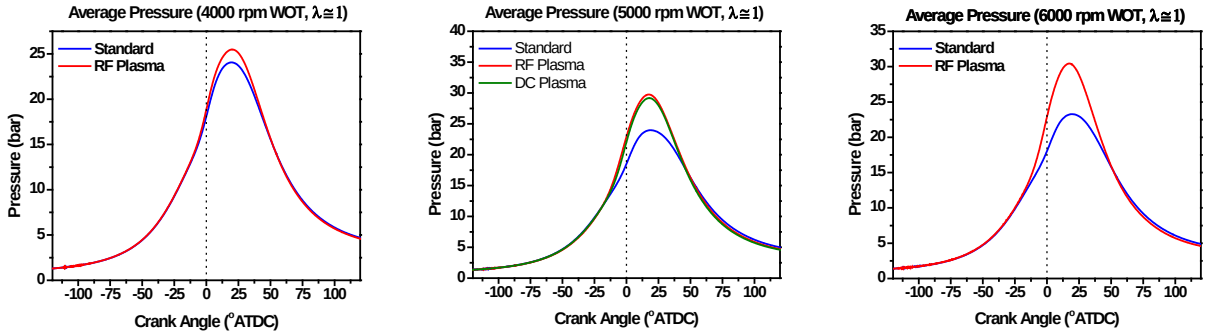

(a) (b) (c)

Figure 20 Pressure trace comparisons of stoichiometric air fuel ratio at a) 4000 revs/min WOT, b) 5000 revs/min WOT, c) 6000 revs/min WOT

6 Optical Engine Testing

Tests of the RF plasma system were conducted in one of Michigan State University's optical engine test cells.

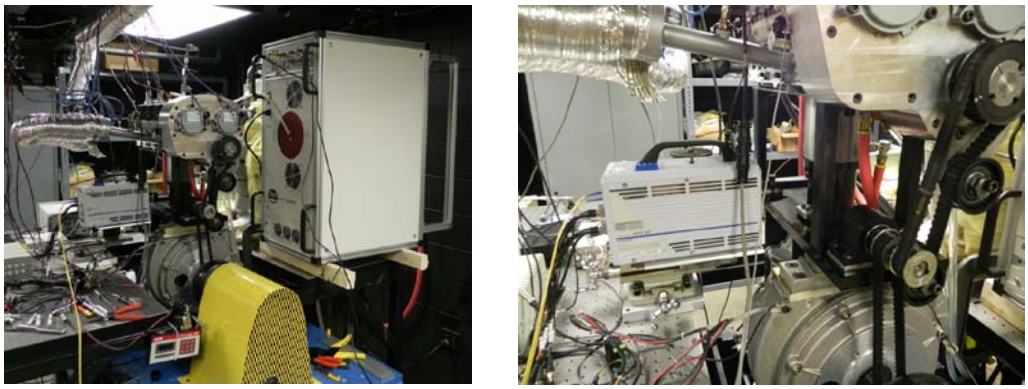

Figure 21 Optical Engine Setup

The RF system tests were compared to tests taken using the optical engine's standard inductive coil. Setup of the testing is shown in Figure 21. The optical engine is a single cylinder engine adapted from a 4 cylinder Chrysler engine. The cylinder is equipped with an extended piston that has a quartz window in the top of the piston head that allows optical access of the combustion chamber. The single cylinder has 0.4 liter displacement, a compression ratio of 9.0, and a bore and stroke of 83 x 73.9 mm. It is four stroke directly injected gasoline engine with a water heated cylinder head. The engine is fully equipped with data acquisition hardware and software that provides calculation of IMEP, λ, cylinder pressure traces, and other relevant

engine parameters. Testing consisted of motoring the engine up to speed followed by 40 engine firing cycles. The high speed camera captured images at every 0.9 crank angle degrees. Tests were run at 1500 rpm with a target engine load of 4.5 bar net IMEP at $\lambda = 1$. By modifying the engine's fuel injection duration and throttle setting, λ sweeps were performed and a flammability limit (engine operating without misfires) for the two ignition systems were determined at the 1500 rpm speed.

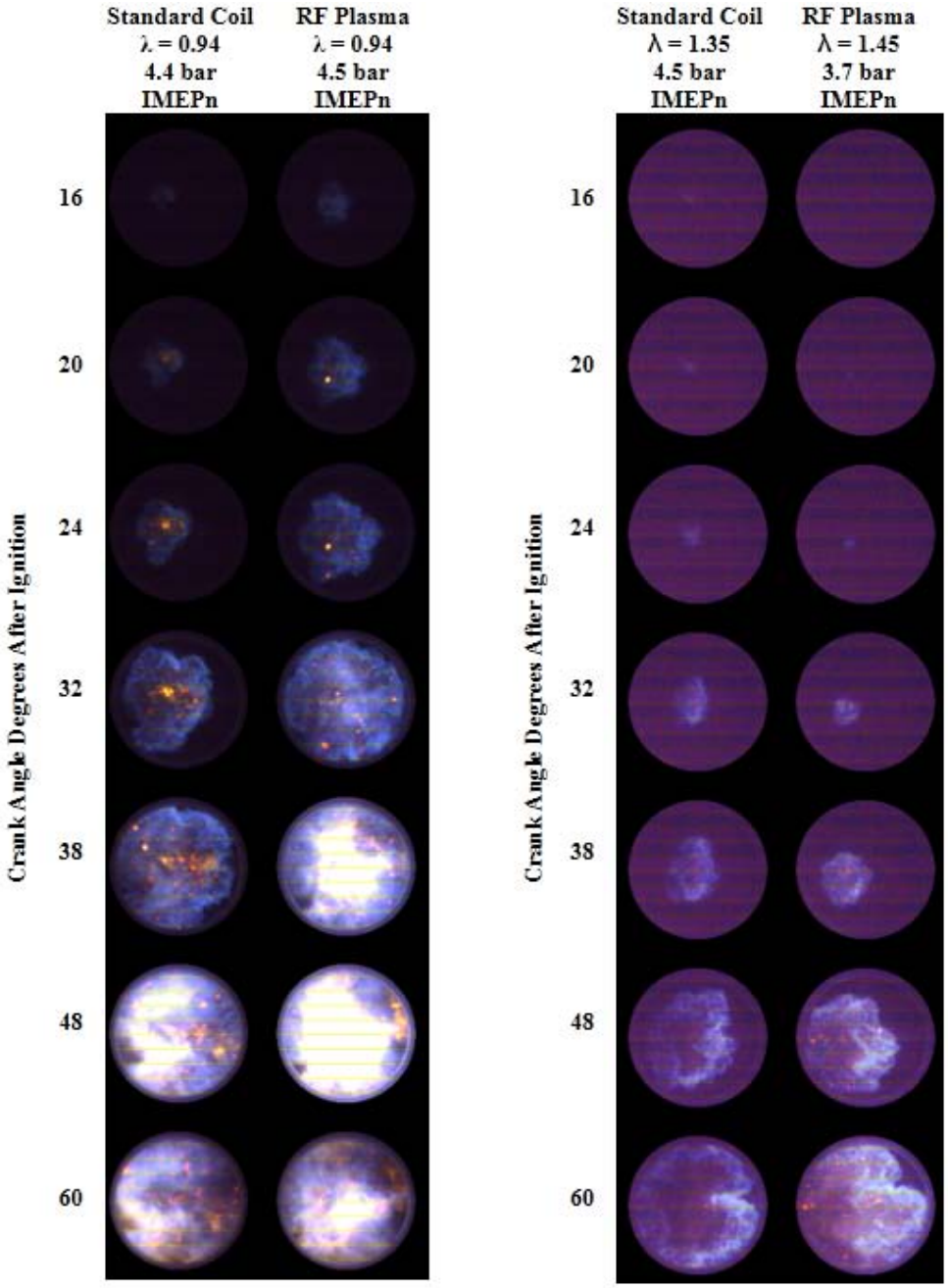

Figure 22 Images from optical engine test runs, (left) rich air fuel conditions, (right) lean limit for each ignition system.

Figure 22 contains photographs taken in the optical engine using the engine's standard ignition coil and the enhanced RF plasma system. Each column is a series of images from a separate engine test with its test conditions specified directly above it. The left two columns of images show the results of test conditions run at rich air fuel conditions. The right two columns of images show the optical tests run at the lean limit of each system. The leanest air fuel mixture achieved for the standard coil was $\lambda = 1.30$ while the leanest mixture achieved without misfires was $\lambda = 1.45$ with the RF system. The tests in the optical engine matched the results from the small engine testing that was performed in improving the engine's ability to tolerate lean air fuel mixtures. The pictures of the rich combustion show a comparison of the flame propagation in the engine between the two ignition systems. Particular attention should be paid to the comparative sizes of the flame kernels at equivalent crank angles between the two tests. It is clear that the flame front is propagating faster and that the combustion at 48° after ignition appears more intense.

7 IMPACT OF PLASMA ON IGNITION CHEMISTRY

In order to understand the impact of the plasma discharge on the flame chemistry, separate laboratory experiments were conducted and scrutinized using laser and optical diagnostics in a microwave plasma torch [33]. The introduction of added species and charged particles (in addition to new reaction chemistry involving ions and electrons) gives rise to new chemical pathways which ultimately results in a higher concentration of radicals, including the representative OH through reactions such as $O(^3P)+H_2O \rightarrow OH+ OH$ and/or $O(^1D)+H_2O \rightarrow OH+OH$ [34]. The sources of O (^3P) and O(^1D) are believed to be mainly from $O_2+e \rightarrow O(^3P)+ O(^1D)+e$ [35], often involving the Herzberg and Schumann-Runge system of the O_2 molecule.

Figure 23 shows a series of images for this the ignition process of a methane and oxygen mixture using a 20 Watt microwave plasma discharge with a flow rate of 100 SCCM and an equivalence ratio of 1.1. The number on top of each image is the time, in ms, starting at the onset of emission from the oxidation reactions. The images were taken at repetitive rate of 10,000 Hz with exposure time of 50 μs. In a very short time after the first image, a faint 'ghost' flame quickly forms and then evolves to a smaller structure as the flame speed grows and the flame is stabilized. This effect is mainly due to the initial breakdown of methane by the discharge through electron impact reactions, but the full effects of the plasma energy have yet to penetrate into the flame zone. After 25 ms, the plasma energy starts to couple into the flame which leads to a larger flame structure and reduction of the glow from the plasma discharge. The flame continues to grow in size and the total time for full stabilization in Figure 23 is about 900 ms. In engine conditions, this is expected to be reduced an order of magnitude.

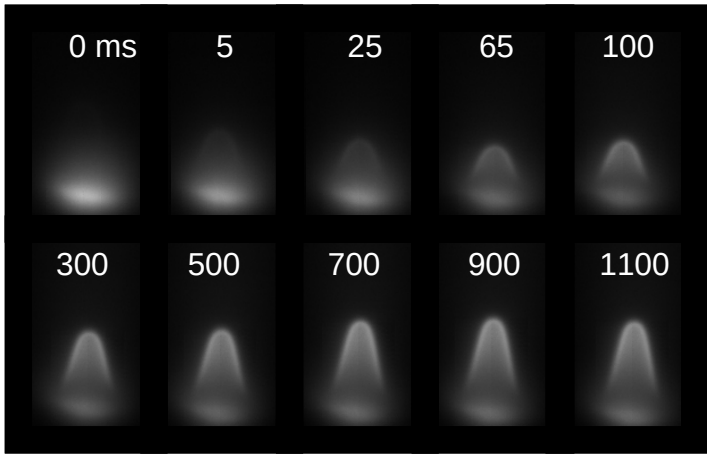

Figure 23 Ignition process of methane and oxygen in a 20 Watt microwave plasma with a flow rate of 100 SCCM with equivalence ratio of 1.1

Experiments with different microwave powers have yielded similar results and the stabilization time for microwave power between 10 and 30 Watts is summarized in Table 1. As expected, the stabilization time becomes smaller with higher microwave power as the higher discharge power and more radical concentration stabilize the ignition process faster. Our observations show that at higher flowrates reveal that the initial flame 'ghost flame' propagation cannot sustain the cascade of electrons which lead to a larger scale radical propagation. In summary, the results show that the ignition occurs in a two step process of initiating a fast pyrolysis flame which in turns initiates the direct coupling of the plasma energy for full ignition to occur.

Microwave Power	W	0	5	10	15	20	25	30
Microwave Air Discharge Volume	mm^3	0	0	35.8	68.2	106.75	214.2	387.1
N_2 rotational temperature	K	n/a	n/a	515	535	580	665	765
Thermocouple Temperature	K	n/a	n/a	618	643	681	713	733
Stabilization Time	ms	n/a	n/a	1,000	940	900	870	850

Table 1 Microwave Discharge Parameters for Powers between 0 and 30 Watts

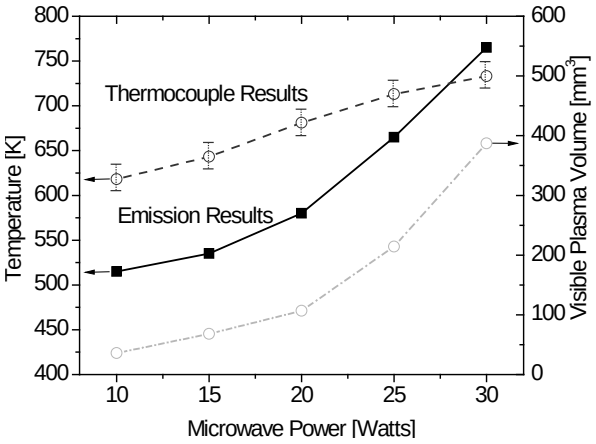

Figure 24: Temperature (thermocouple and rotational N_2 emission of the microwave air discharge with different power levels (left Y axis); visible plasma volume with different power levels (right Y axis).

It can also be seen from table 1 that ignition occurs mainly under conditions below the auto-ignition temperature. Figure 24 shows various temperature measurements made in the plasma plume that ignition condition s below 30 W indeed measure below the auto-ignition temperature of methane. Regardless of the temperature results, it could be argued that there are localized hot spots at the micron scale which can contribute as local ignition sites, and further accelerated through electron and ion impact reactions from the plasma. It is clear from these results however that stable ignition of the fuel air mixture can occur with lower thermal energy transfer using a non-equilibrium plasma discharge and first order calculations attribute about 35% of the ignition energy to be coming from ohmic heating of the fuel and oxider mixture.

Another significant mechanism for acceleration of the flame chemistry is through in-situ fuel reforming as shown by [22]. In order to measure the contribution of fuel breakup to syngas, we have measured the CO number densities by using two photon laser induced fluorescence spectroscopy [33,36] which has been quantitatively calibrated from Chemkin simulations using GRI-mech 3.0 [37] with 1-D flame modeling of methane and oxygen. Overall CO number density increases with microwave power. Prior to full initiation of the radical propagation, the weak impact of the plasma and in-situ fuel reforming (to hydrogen and carbon monoxide) as well as the temperature increase is expected to contribute to enhancement in ignition flammability limits and flame speed. As the main thermal oxidation takes place, in-situ fuel reforming is seen to dramatically increase. Calculations show that in our configuration, 18% of the total methane undergoes reforming to syn-gas at 30W of microwave power, which is

significant considering the competing oxidation reactions which subsequently leads to CO_2.

In conclusion, it can be speculated that enhanced ignition in an engine using a plasma discharge is a combined impact of localized hot spots and ohmic heating, pre-dissociation of fuel due to fast electron impact reactions, enhanced chemical pathways via new electron and ion impact reactions, as well as in-situ fuel reforming.

8 CONCLUSION

Two groups of undergraduate mechanical engineering students at Michigan State University were provided the opportunity to significantly contribute to the research related tasks associated with this study. Through this research program, the students were able to participate in the activity of designing, building, and troubleshooting the small engine test rig constructed for this project using their opportunity as a means to gain experience in applying their engineering knowledge to practical problems and gaining exposure to a field of active research. Some of the students were also able to take advantage of the opportunity to visit the SERL at Wright Patterson Air Force Base to present their work at the University Capstone Project Demonstration Day held there earlier this year in June.

A small engine dynamometer test stand with a capacity of 7.0 kW has been successfully built. An engine identical to a Fuji Imvac-34EI engine has been installed with the necessary instrumentation to collect engine test data from it in the test rig and is reliably coupled to the dynamometer. A high quality radio frequency AC plasma ignition system was designed and built. A second commercially available DC nanosecond pulse plasma system was obtained, and the two systems were tested in the small engine. Comparison of the small engine tests performed with the engine's standard spark discharge system and the two plasma systems showed improved power output and combustion stability was obtained at identical λ with the plasma systems. The test also show that the plasma systems tolerate lean air fuel mixtures much better than the standard coil as the difference in performance between the standard system and the plasmas becomes more dramatic as λ increases. It is clear from these tests that both the RF plasma and the DC nanosecond plasma have the potential to permit the small engine to operate with leaner air fuel mixtures while maintaining the equivalent performance in terms of the power output produced by the standard spark at rich or stoichiometric conditions. The pressure rise rates also indicate that the rate of combustion is faster when the plasma systems are used attributing to their improved performance. It is also important to note that while both plasma systems outperformed the standard coil system, the RF system outperformed the DC system slightly.

Finally, optical engine testing was also performed using the RF system and compared to tests run using a standard spark ignition system. These tests serve to reinforce the findings from the small engine testing as the plasma system provided better lean mixture performance. Images from the testing also appear to display larger flame kernels and faster flame propagation at similar λ values for the RF system.

9 ACKNOWLEDGEMENTS

Much of the work discussed here was carried out in collaboration with the Propulsion Directorate at Wright Patterson Air Force Base. In particular, we are grateful for the helpful guidance of Dr. Frederick R. Schauer and Dr. Paul J. Litke in the Gas Turbine Division of the Propulsion Directorate at Wright Patterson Air Force Base. We are grateful for the support from

AFOSR and AFRL which has resulted in this work as well as the Honors College at Michigan State University.

10 PERSONNEL SUPPORTED

Faculty

Professor Tonghun Lee, George Zhu, Harold Schock

Graduate Students (part support)

Bryce Thelen (Ph.D. student), Stephen Hammack (Ph.D. student), Xing Rao (Ph.D. student)

Indergraduate Students

Curt Mumaw, Garret Kerns, Joseph Rotellini, Stephen Santavicca, Jonathan DiClemente, Tomas Hallahan, Gregory Tenbusch, Adam Sajdak (Junior & Senior Level)

11 PUBLICATIONS FROM THIS GRANT

1. S. Hammack, J. Gord, C. Carter, T. Lee, Nitric Oxide PLIF at 10 kHz in a seeded flow, a plasma discharge, and a flame, Optics Letters, accepted and in print (2012)
2. S. Hammack, C. Carter, T. Lee, Microwave Plasma Enhancement of Various Flame Geometries at Atmospheric Pressure, IEEE Transactions, Special Issue on Plasma Science, 99, 1-8 (2012)
3. S. Hammack, C. Carter, T. Lee, Direct Coupled Plasma Assisted Combustion using a Microwave Waveguide Torch, IEEE Transactions, Special Issue on Plasma Science, 39, 12, 3300-3306 (2011).
4. X. Rao, S. Hammack, T. Grotjohn, J. Asmussen, C. Carter, T. Lee, Microwave Plasma Coupled Re-Ignition of Methane and Oxygen Mixture under Auto-Ignition Temperature, IEEE Transactions, Special Issue on Plasma Science, 39, 12, 3307-3313 (2011).
5. X. Rao, S. Hammack, C. Carter, T. Lee, Laser Diagnostics Imaging of Energetically Enhanced Flames using Direct Microwave Plasma Coupling, IEEE Transactions on Plasma Science, 39, 11, 2354-2355 (2011).
6. S. Hammack, X. Rao, C. Carter, Z. Williamson, T. Lee, Laser Diagnostics of Plasma Enhanced Flames in a Waveguide Microwave Discharge System, 49th Aerospace Sciences Meeting, Orlando FL, Jan., AIAA-2011-1019 (2011).
7. X. Rao, S. Hammack, C. Carter, I. Matveev, T. Lee, Combustion Dynamics of Plasma Enhanced Premixed and Non-Premixed Flames, IEEE Transactions, Special Issue on Plasma Science, 38, 12, 3265-3271, (2010).

12 REFERENCES

1. A. Y. Starikovskii, "Plasma supported combustion," Proc. Comb. Inst. **30,** 2405-2417 (2005).
2. S. M. Starikovskaia, "Plasma assisted ignition and combustion," Journal of Physics D: Applied Physics **39,** R265-R299 (2006).
3. S. B. Leonov, and D. A. Yarantsev, "Plasma-induced ignition and plasma-assisted combustion in high-speed flow," Plasma Sources Science and Technology **16,** 132-138 (2007).
4. K. W. Hemawan, C. L. Romel, S. Zuo, I. S. Wichman, T. A. Grotjohn, and J. Asmussen, "Microwave plasma-assisted premixed flame combustion," Appl. Phys. Lett. **89,** 141501 (2006).
5. F. Wang, J. B. Liu, J. Sinibaldi, C. Brophy, A. Kuthi, C. Jiang, P. Ronney, and M. A. Gundersen, "Transient Plasma Ignition of Quiescent and Flowing Air/fuel Mixtures," IEEE Trans. on Plasma Science **33,** 844-849 (2005).
6. J. Lawton, and F. J. Weinberg, Electrical Aspects of Combustion, (Clarendon, Oxford, 1969).
7. H. C. Jaggers, and A. von Engel, "The effect of electric fields on the burning velocity of various flames," Combustion and Flame **16,** 275-285 (1971).
8. F. B. Carleton, I. M. Vince, and F. J. Weinberg, "Energy and radical losses from plasma jet igniters to solid surfaces," Proc. Comb. Inst. **19,** 1523-1531 (1982).
9. A. J. J. Lee, and F. J. Weinberg, "A novel ignition device for the internal combustion engine," Nature (London, United Kingdom) **311,** 738-740 (1984).
10. F. J. Weinberg, K. Hom, A. K. Oppenheim, and K. Teichman, "Ignition by plasma jet," Nature **272,** 341-343 (1978).
11. L. Bromberg, D. R. Cohn, A. Robinovich, and N. Alexeev, "Plasma Catalytic Reforming of Methane," Inter. J. of Hydrogen Energy **24,** 1131-1137 (1999).
12. C. S. Kalra, A. Gutsol, and A. Fridman, "Gliding arc discharge as a source of intermediate plasma for methane partial oxidation," IEEE Transactions on Plasma Science **33,** 32-41 (2005).
13. G. Lou, A. Bao, M. Nishihara, S. Keshav, Y. G. Utkin, J. W. Rich, W. R. Lempert, and I. V. Adamovich, "Ignition of Premixed Hydrocarbon-Air Flows by Repetitively Pulsed, Nanosecond Pulse Duration Plasma," Proc. Comb. Inst. **31,** 3327-3334 (2007).
14. W. Kim, H. Do, M. G. Mungal, and M. A. Capelli, "Flame stabilization enhancement and NOx production using ultra short repetitively pulsed plasma discharge," in *44th AIAA Aerospace Sciences Meeting and Exhibit, AIAA-2006-560* (2006).
15. T. Ombrello, X. Qin, Y. Ju, A. Gutsol, A. Fridman, and C. Carter, "Combustion Enhancement via Stabilized Piecewise Nonequilibrium Gliding Arc Plasma Discharge," AIAA J. **44,** 142-150 (2006).
16. W. Kim, H. Do, M. G. Mungal, and M. A. Cappelli, "Plasma-Discharge Stabilization of Jet Diffusion Flames," IEEE Transactions on Plasma Science **34,** 2545-2551 (2006).
17. N. Chintala, A. Bao, G. Lou, and I. V. Adamovich, "Measurements of combustion efficiency in nonequilibrium RF plasma-ignited flows," Combustion and Flame **144,** 744-756 (2006).
18. A. B. Leonov, D. A. Yarantsev, A. P. Napartovich, and I. V. Kochetov, "Plasma-assisted ignition and flameholding in high-speed flow," in *44th AIAA Aerospace Sciences Meeting, AIAA-2006-563*, AIAA-2006-563 (Reno, Nevada, 2006).

19. T. Kitagawa, A. Moriwaki, K. Murakami, K. Takita, and G. Masuya, "Ignition characteristics of methane and hydrogen using a plasma torch in supersonic flow," Journal of Propulsion and Power **19,** 853-858 (2003).
20. I. Matveev, S. Matveeva, A. Gutsol, and A. Fridman, "Non-Equilibrium Plasma Igniters and Pilots for Aerospace Applications," in *43rd AIAA Aerospace Sciences Meeting and Exhibit, AIAA Paper 2005-1191* (Reno, 2005).
21. I. Kimura, "Effectiveness of Plasma Torches for Ignition and Flameholding in Scramjet," Journal of Propulsion and Power **8** (1992).
22. W. Kim, M. Godfrey Mungal, and M. A. Cappelli, "The role of in situ reforming in plasma enhanced ultra lean premixed methane/air flames," Combustion and Flame **157,** 374-383 (2009).
23. J. B. Liu, P. D. Ronney, and M. A. Gundersen, "Premixed flame ignition by transient plasma discharges," Proc. Combust. Inst **29,** 21-26 (2002).
24. Y. D. Korolev, and I. B. Matveev, "Nonsteady-State Processes in a Plasma Pilot for Ignition and Flame Control," Plasma Science, IEEE Transactions on **34,** 2507-2513 (2006).
25. L. Bromberg, D. R. Cohn, A. Rabinovitch, and J. Heywood, "Emissions Reductions Using Hydrogen from Plasmatron Fuel Coverters," Inter. J. of Hydrogen Energy **26,** 1115-1121 (2001).
26. S. H. Zaidi, E. Stockman, X. Qin, Z. Zhao, S. Macheret, Y. Ju, R. B. Miles, D. J. Sullivan, and J. F. Kline, "Measurements of hydrocarbon flame speed enhancement in high-Q microwave cavity," in *44th AIAA Aerospace Sciences Meeting and Exhibit, AIAA-2006-1217* (2006).
27. C. D. Cathey, T. Tang, T. Shiraishi, T. Urushihara, A. Kuthi, and M. A. Gundersen, "Nanosecond plasma ignition for improved performance of an internal combustion engine," Plasma Science, IEEE Transactions on **35,** 1664-1668 (2007).
28. S. Memarzadeh, J. Colgrove, and P. Ronney, "Transient Plasma Discharge Ignition for Internal Combustion Engines," in *d Int. Workshop and Exhibition on Plasma Assisted Combustion, Falls Church, USA* (2007), pp. 47-48.
29. J. A. Bittencourt, Fundamentals of plasma physics 3rd ed., (Springer, 2003).
30. J. Meichsner, "Low Temperature Plasmas," Plasma Physics **670,** 95 (2005).
31. A. A. Tropina, L. Lenarduzzi, S. V. Marasov, and A. P. Kuzmenko, "Comparative analysis of engine ignition systems," Plasma Science, IEEE Transactions on **37,** 2286-2292 (2009).
32. J. B. Heywood, "Internal combustion engine fundamentals, 1988," (McGraw-Hill, New York, 2002).
33. X. Rao, S. Hammack, C. Carter, T. Grotjohn, J. Asmussen, and T. Lee, "Microwave-Plasma-Coupled Re-Ignition of Methane-and-Oxygen Mixture Under Auto-Ignition Temperature," Plasma Science, IEEE Transactions on **39,** 3307-3313 (2011).
34. R. Ono, and T. Oda, "OH radical measurement in a pulsed arc discharge plasma observed by a LIF method," IEEE Transaction on Industry Applications **37,** 709-714 (2001).
35. B. Eliasson, M. Hirth, and U. Kogelschatz, "Ozone synthesis from oxygen in dielectric barrier discharges," J. Phys. D: Appl. Phys. **20,** 1421 (1986).
36. X. Rao, S. Hammack, T. Lee, C. Carter, and I. B. Matveev, "Combustion Dynamics of Plasma-Enhanced Premixed and Nonpremixed Flames," Plasma Science, IEEE Transactions on **38,** 3265-3271 (2010).
37. M. Tamura, J. Luque, J. E. Harrington, P. A. Berg, G. P. Smith, J. B. Jeffries, and D. R. Crosley, "Laser-induced fluorescence of seeded nitric oxide as a flame thermometer," Appl.

Phys. B **66,** 503-510 (1998).